

Role of Synthesis on Physical Properties of $\text{Ni}_{0.5}\text{Zn}_{0.5}\text{Fe}_2\text{O}_4$ Nanoferrite: A Comparative Study

B. Rajesh Babu¹  · M. S. R. Prasad² · K. V. Ramesh³

Received: 30 October 2016 / Accepted: 23 December 2016 / Published online: 7 January 2017
© Springer Science+Business Media New York 2017

Abstract In this work, $\text{Ni}_{0.5}\text{Zn}_{0.5}\text{Fe}_2\text{O}_4$ nanoparticles have been synthesized by coprecipitation, sol-gel and citrate-gel auto combustion wet chemical methods. The as-synthesized samples were sintered at 1073 K and characterized by X-ray diffraction (XRD), Scanning electron microscope (SEM), Fourier transform infrared spectroscopy (FTIR), Vibrational sample magnetometer (VSM), and DC electrical resistivity. Analysis of x-ray diffraction patterns confirm the formation of single-phase cubic spinel structure for all the sintered samples under study. IR measurements also support the formation of spinel phase of the synthesized samples. Saturation magnetization has been found to be increased after sintering. Results showed that Ni–Zn ferrite prepared through Citrate-gel auto combustion method has maximum saturation magnetization, stable permeability, and high electrical resistivity.

Keywords Ni–Zn nanoferrite · Citrate-gel auto combustion · XRD · IR spectra · Saturation magnetization

1 Introduction

More than half of the century, spinel ferrites have been extensively investigated due to their remarkable magnetic

and electrical properties. High-saturation magnetization, electrical resistivity, low electric loss, and chemical stability make them useful for wide range of applications. Among the spinel ferrites, Ni–Zn ferrite is an excellent core material for power transformers in electronic and telecommunication applications. Current developments in the field of power electronic devices are leading to miniaturization. A size reduction is usually possible by increasing the operating frequency and the initial permeability. The frequency of operation of these ferrites is directly proportional to square of saturation magnetization, electrical resistivity and inversely related to the grain size [1].

The structural, magnetic, and electrical properties of spinel ferrites are sensitive to microstructure, which in turn significantly depends on synthesizing method. In earlier days, Ni–Zn ferrites are prepared by conventional ceramic method. In this process, high temperature and long sintering times are required for better atomic mobility. However, this prolonged heating at elevated temperatures favorable for volatilization of some of the elements, leading to composition gradient, produce low surface area and undesirable crystal growth [2, 3]. Thus, the obtained final products are non-reproducible with coarser grain size, which limits their performance to megahertz frequency. For this reason, several researchers developed different preparation routes to produce stoichiometric spinel ferrites with desired properties.

Recently, spinel ferrites are synthesized at nanoscale, which opens a new and exciting research filed, with numerous applications in electronic technology [4]. The pertinent reason is due to the drastic changes in the electrical and magnetic properties when the size of the particle is reduced to nanoscale. Several authors reported on the synthesis of nano-sized spinel ferrites using a variety of wet chemical methods like auto combustion synthesis [5],

✉ B. Rajesh Babu
rajeshbabu.bitra@gmail.com

¹ Department of Physics, G.V.P. College of Engineering for Women, Visakhapatnam, India

² Department of Physics, MVGR College of Engineering, Chintalavalasa, Vizianagaram, India

³ Department of Physics, GIS, GITAM University, Rushikonda, Visakhapatnam, India

co-precipitation [6], sol-gel [7], microwave sintering [8], and hydrothermal [9] routes to synthesize homogeneous, fine and reproducible ferrites. In addition, material scientists and solid-state researchers are still curious to develop new routes to synthesize nanocrystalline spinel ferrites with improved electrical and magnetic properties due to the possible manipulation of matter at the molecular level and control over the particle size. On the other hand, achieving superior electromagnetic properties at low sintering temperature is also a tough challenge.

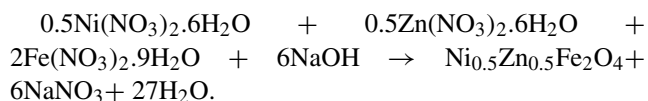
In this view of above-mentioned facts, it is thought that a systematic comparative study would be very much useful and essential in emerging nanotechnology. The present article highlights the role of preparation method on structural, magnetic, and electrical properties of Ni–Zn nano ferrites synthesized via different wet-chemical routes.

2 Experimental

2.1 Preparation Methods

2.1.1 Coprecipitation Method

$\text{Ni}_{0.5}\text{Zn}_{0.5}\text{Fe}_2\text{O}_4$ nanoparticles have been synthesized by using coprecipitation method according to the following chemical route:

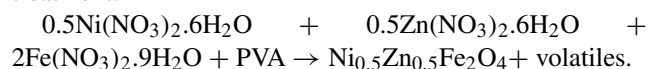


Required stoichiometric amounts Ni $(\text{NO}_3)_2 \cdot 6\text{H}_2\text{O}$, Zn $(\text{NO}_3)_2 \cdot 6\text{H}_2\text{O}$, and Fe $(\text{NO}_3)_2 \cdot 9\text{H}_2\text{O}$ were taken as starting materials dissolved separately in deionized water. These solutions are mixed intimately and stirred for half an hour to improve the homogeneity of the solution. The precipitating agent NaOH aqueous solution of 0.5 Mol was prepared and added drop wise to the cationic solution with constant stirring at room temperature. The addition of NaOH leads to the formation of a brown massy precipitate at the bottom of the vessel. The formation of precipitate was found to be in the pH range of 12.5–13. Heating of the precipitate in its alkaline condition was continued at a soaking temperature of 100 °C for 1 h. The final solution was filtered off and the precipitated composite was washed with distilled water repeatedly to remove the salt residues and other impurities. Finally, acetone was used to remove the free water content from the particle surface and dried in an oven at 95 °C to obtain the powder. The coprecipitated ferrite agglomerates were then ground for half an hour to obtain loose powder.

2.1.2 Sol-gel Method

The stoichiometric amounts of iron, nickel, and zinc nitrates were weighed and dissolved in deionized water separately

(precursors). These individual precursors were mixed and stirred for 1 h to achieve homogeneity and the final solution was heated to 60 °C. The required amount of aqueous solution of polyvinyl alcohol is prepared (molar ratio of nitrates to PVA is 1:1) and was added drop by drop to the cationic solution under continuous stirring. As the time proceeds, the gelation continued step by step and a red gel-type massy product thus formed with the release of fume reddish brown gases around 100 °C. At this temperature, the red gel type product slowly converted into a bulky fluffy mass and it was collected for further treatment. The final residue was collected and grounded for 1-h further treatment.



2.1.3 Citrate-gel Autocombustion Method

According to the chemical formula, $\text{Ni}_{0.5}\text{Zn}_{0.5}\text{Fe}_2\text{O}_4$ sample is prepared through citrate-gel auto combustion route, using Ni, Zn, and Fe metal nitrates as starting compositions. The stoichiometric metal nitrate compounds were weighed and dissolved in deionized water separately. Citric acid aqueous solution (molar ratio of citric acid to metal nitrates solution is 1:1) was added to the metal nitrates solution to chelate (A chelating agent is a substance whose molecules can form several bonds to a single metal ion, i.e., chelating agent is a multidentate ligand) Ni^{2+} , Zn^{2+} and Fe^{3+} in the solution. At the temperature about 100 °C, the solution boiled and froths due to dehydration and under continuous elimination of water, the solution then slowly transformed to a gel. Gelation continued in a step process with further liberation of water molecules and the thickness of the gel slowly increased until a red-type viscous gel was formed with evolution of reddish brown gases and the gel subsequently self ignited. Upon ignition, the dried gel burns in a self-propagating combustion manner until the total gel is completely burnt out and gave rise to a fluffy, dry massy residue. The reaction is self-propagating and is able to sustain this from 1 to 5 s typically, to form the desired product. The as-burnt powders are collected and ground using an agate mortar and pestle for 1 h to obtain a loose ferrite powder. $\text{Ni}_{0.5}\text{Zn}_{0.5}\text{Fe}_2\text{O}_4$ samples synthesized through coprecipitation, sol-gel, and citrate-gel methods are designated as S1, S2, and S3, respectively.

2.2 Characterization Techniques

As-synthesized $\text{Ni}_{0.5}\text{Zn}_{0.5}\text{Fe}_2\text{O}_4$ nano powders obtained from coprecipitation, sol-gel, and citrate-gel auto combustion methods were sintered at 1073 K for 4 h. These samples were subjected to various characterization techniques to study their structural, magnetic, and electrical properties.

The powder x-ray diffraction (XRD) patterns were recorded on the Pan-analytical X'Pert-PRO diffractometer using Cu-K α radiation ($\lambda = 1.5406 \text{ \AA}$) at room temperature. Infrared spectra have been recorded using Shimadzu Prestige-21 FT-IR spectrometer in the standard KBr medium at room temperature within the wave number range of 300 to 700 cm^{-1} . Room temperature M-H loops were recorded on Lakeshore vibrational sample magnetometer (VSM) magnetometer (model: 7410) for a maximum magnetic field of 1.5 Tesla. Permeability measurements were done on the Impedance Analyzer (Model: PSM 1735) for a small voltage of 1 mV in the frequency range of 1 kHz to 13 MHz. DC resistivity measurements were carried out on pellets (10 mm in diameter, 4 mm in thickness) at room temperature using two-probe method.

3 Results and Discussion

3.1 Phase Analysis and Lattice Constant

The x-ray diffraction patterns of as-prepared $\text{Ni}_{0.5}\text{Zn}_{0.5}\text{Fe}_2\text{O}_4$ samples shown in Fig. 1. It is observed that $\text{Ni}_{0.5}\text{Zn}_{0.5}\text{Fe}_2\text{O}_4$ prepared through sol-gel and citrate-gel methods exhibit cubic spinel phase. Figure 2 shows the x-ray diffraction patterns of $\text{Ni}_{0.5}\text{Zn}_{0.5}\text{Fe}_2\text{O}_4$ samples sintered at 1073 K. The diffraction peaks corresponding to (220), (311), (222), (400), (422), (511), and (440) match well with reflections of the nickel-zinc ferrite reported in the standard card (JCPDS card no.: 08-0234). The broader

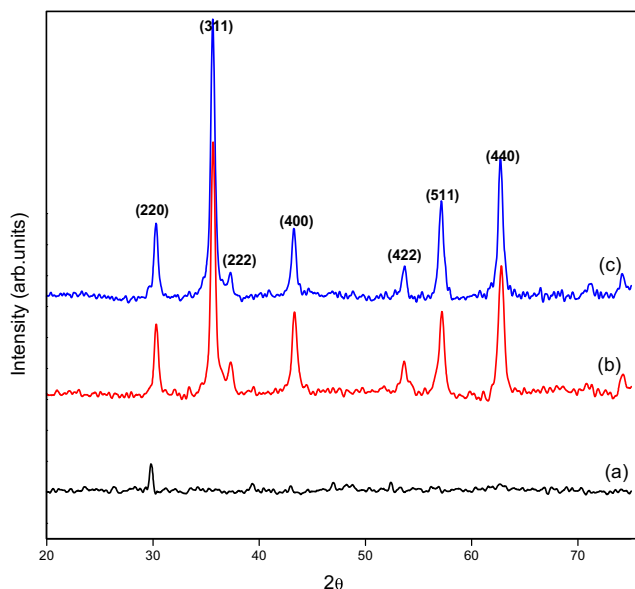


Fig. 1 X-ray diffractograms of as prepared $\text{Ni}_{0.5}\text{Zn}_{0.5}\text{Fe}_2\text{O}_4$ samples prepared through **a** coprecipitation, **b** sol-gel, and **c** citrate-gel methods

diffraction peaks suggest the nano crystalline nature of the materials. It is evident that the as-prepared (Fig. 1) and sintered (Fig. 2) samples processed through sol-gel and citrate gel methods resulted in required nanoparticles of single spinel phase, whereas after sintering for coprecipitation sample (Fig. 2). The wet chemical method is relatively low-temperature processing, faster, and economical compared to the conventional ceramic method. However, in the present case, it is observed that heat treatment is required for the samples processed through coprecipitation method. The lattice constant (a) for cubic system was calculated using

$$a = d\sqrt{h^2 + k^2 + l^2} \quad (1)$$

where h , k , and l are the Miller indices, and d is the interplanar spacing. Accurate lattice parameter has been obtained by plotting a graph between lattice parameter versus Nelson-Riley function, $F(\theta)$ [10]. Figure 3 shows Nelson-Riley plots of $\text{Ni}_{0.5}\text{Zn}_{0.5}\text{Fe}_2\text{O}_4$ samples sintered at 1073 K and the calculated lattice constants are shown in Table 1.

3.2 Crystallite Size and Lattice Strain

The mean crystallite size D has been calculated from the experimentally observed broadening of the most intense (311) x-ray diffraction peak using Debye-Scherrer equation [11]

$$D_{311} = \frac{k\lambda}{\beta\cos\theta} \quad (2)$$

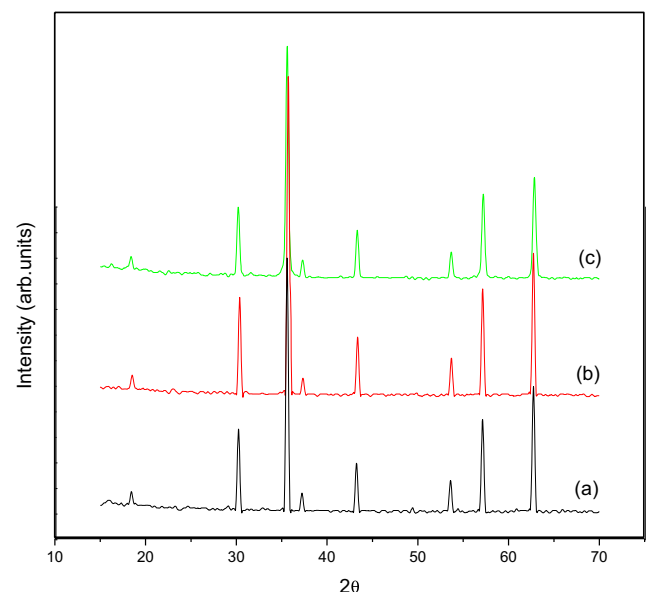


Fig. 2 X-ray diffractograms of $\text{Ni}_{0.5}\text{Zn}_{0.5}\text{Fe}_2\text{O}_4$ samples sintered at 1073 K prepared through **a** coprecipitation, **b** sol-gel, and **c** citrate-gel methods

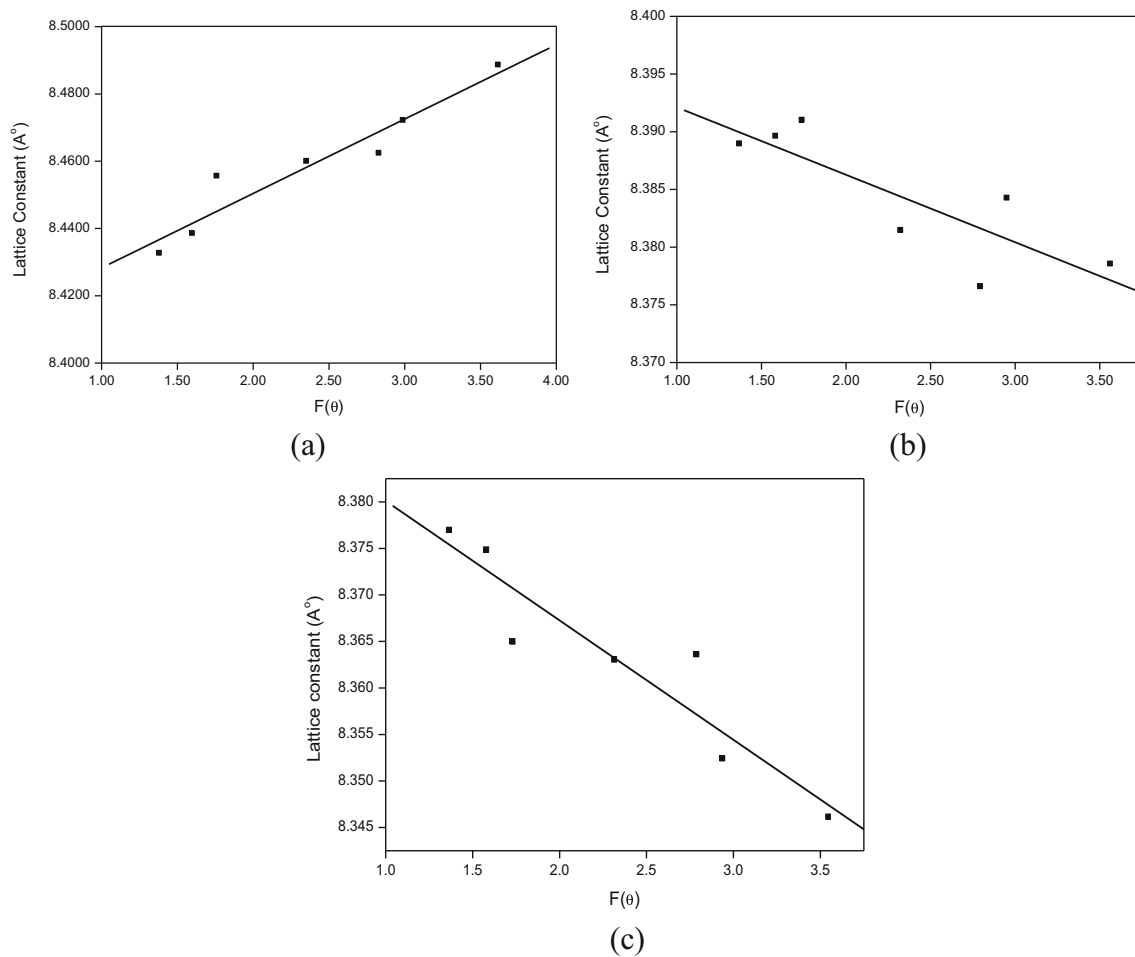


Fig. 3 Nelson-Riley plots of $\text{Ni}_{0.5}\text{Zn}_{0.5}\text{Fe}_2\text{O}_4$ samples sintered at 1073 K prepared through **a** coprecipitation, **b** sol-gel, and **c** citrate-gel methods

where k is the Scherrer factor (0.9), λ is the wavelength of $\text{Cu-K}\alpha$ radiation (1.5406 Å), and β is the full width at half maximum (FWHM) in radians. The average crystallite size ($D_{\text{W-H}}$) is also estimated from Williamson-Hall method, where one can easily separate crystallite size and microstrain and the procedure has been given elsewhere [12]. XRD peaks are broaden due to (1) instrumental effect, (2) smaller crystallite size, and (3) lattice strain in the material. The lattice strain (η) has been calculated using the relation

which is obtained by modifying the Williamson and Hall equation

$$\eta = \frac{2d|(k-1)|}{D} \quad (3)$$

where d is the lattice spacing for (311) planes, D is the average crystallite size, and k (0.9) is the shape factor. The average crystallite size of as-prepared, sintered samples and lattice strain are shown in Table 1. In general, crystallite size

Table 1 Lattice constant (a), average crystallite size Scherrer (D_{311}), and W-H method ($D_{\text{W-H}}$) nanometers of as-prepared and sintered at 1073 K $\text{Ni}_{0.5}\text{Zn}_{0.5}\text{Fe}_2\text{O}_4$ samples

Parameter	As prepared/sintered	Coprecipitation (S1)	Sol-gel (S2)	Citrate-gel (S3)
Lattice constant	As prepared	–	8.3874	8.3903
a (± 0.004) Å	1073K	8.4062	8.3979	8.3929
Average crystallite size (D_{311}) nanometer	As prepared	–	23	30
	1073K	37	20	24
Average crystallite size ($D_{\text{W-H}}$) nanometer	As prepared	–	20	25
	1073K	33	17	28
Lattice strain (η)	As prepared	–	0.0218	0.0201
	1073K	0.0138	0.0228	0.0179

Table 2 Cationic distribution estimated from intensity calculations (S1 coprecipitation, S2 sol-gel, S3 citrate-gel method)

Sample	A site	B site	I_{220}/I_{400}		I_{220}/I_{422}		I_{422}/I_{400}	
			Obs.	Cal.	Obs.	Cal.	Obs.	Cal.
S1	$Zn_{0.5}Fe_{0.5}$	$Ni_{0.5}Fe_{1.5}$	0.775	0.873	0.775	0.798	1.777	1.012
S2	$Zn_{0.465}Fe_{0.54}$	$Zn_{0.035}Ni_{0.5}Fe_{1.465}$	0.829	0.878	0.881	0.804	1.849	1.013
S3	$Zn_{0.5}Fe_{0.5}$	$Ni_{0.5}Fe_{1.5}$	0.848	0.88	0.829	0.803	1.849	1.013

increases with sintering temperature. The observed decrease in crystallite size is ascribed to the increase in lattice strain.

3.3 Cation Distribution

In the present system, Cation distribution was calculated from relative X-ray intensity calculations suggested by Bertaut [13]. Intensity ratios of some peak-pairs in the XRD pattern of spinel structures are known to be sensitive to cation distribution, such as I_{220}/I_{400} , I_{220}/I_{422} , and I_{422}/I_{400} . The intensities of these are nearly independent of the oxygen parameters. The calculations were made for various combinations of cations until a well agreement between observed and calculated intensity ratios are obtained. The distribution of cations among tetrahedral site (A) and octahedral site (B) are shown in Table 2. It is can be seen that Zn^{2+} ions predominantly occupy A sites and Ni^{2+} ions occupy B sites, whereas Fe^{3+} ions are distributed in to both A and B sites. However, in case of S2 sample, a fraction of Zn^{2+} ions migrate in to B-site. The observed decrease in magnetization for the S2 sample compared to as prepared also supports this distribution.

3.4 Infrared Spectra

Room-temperature infrared spectra of as prepared and sintered at 1073 K Ni–Zn ferrite powders are shown in Figs. 4 and 5. According to Waldron [14], IR spectrum consists of two fundamental absorption bands in the wave number range of $400\text{--}600\text{ cm}^{-1}$ corresponding to intrinsic vibrations of Me–O in two different environments (Me–metal ion). The low frequency band (ν_2) concentrated around 400 cm^{-1} is due to stretching of Me–O bonds at octahedral site (B) while the high-frequency band (ν_1) around 600 cm^{-1} corresponds to tetrahedral sites (A). Such difference can be expected due to the difference in the A–O and B–O bond lengths. In tetrahedral complex, bond distance is smaller ($\sim 1.92\text{ \AA}$) than compared to octahedral complex ($\sim 2.03\text{ \AA}$). Smaller bond distance results greater covalence between metal cations and surrounding oxygen ion. Thus, the absorption frequency is high for B sites and low for A sites. Due to the inverse relation between bond length and absorption frequency, one can easily understand the changes occur in the sublattice due to cationic positions. However, in the present work we focused on influence of synthesis

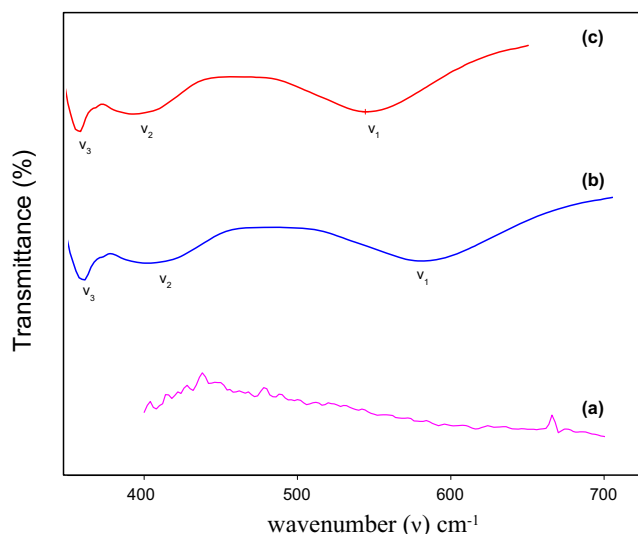


Fig. 4 Infrared spectra of as-prepared $Ni_{0.5}Zn_{0.5}Fe_2O_4$ samples prepared through **a** coprecipitation, **b** sol-gel, and **c** citrate-gel methods

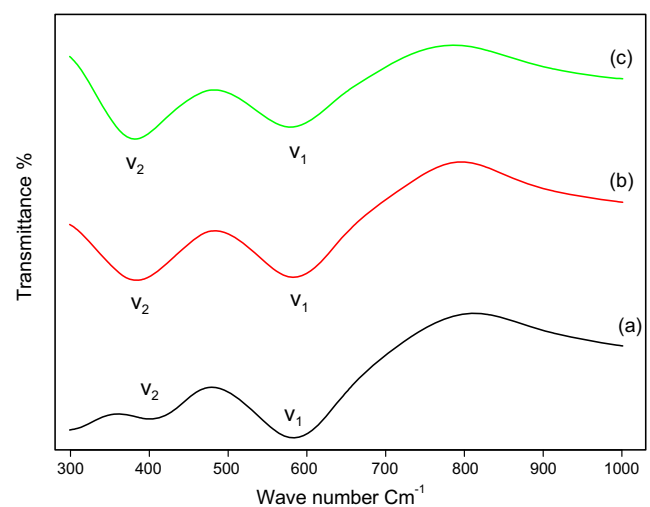


Fig. 5 Infrared spectra of $Ni_{0.5}Zn_{0.5}Fe_2O_4$ samples sintered at 1073 K prepared through **a** coprecipitation, **b** sol-gel, and **c** citrate-gel methods

method. No splitting or presence of additional shoulders in the IR absorption bands corresponding to ν_1 and ν_2 has been observed for all annealed powders which implicates a near absence of the Fe^{2+} ions at both octahedral and tetrahedral sites of the spinel lattice. This is due to the fact that local deformations can occur in the Fe^{2+} ions due to the

Jahn-Teller effect which can lead to a non cubic component of the crystal field potential and hence to splitting of the band which has not been observed in the present study. The presence of an absorption band (ν_3) concentrated around $350\text{--}360\text{ cm}^{-1}$ for the as-prepared powders (S1 and S2) is attributed to the presence of the divalent metal ion in

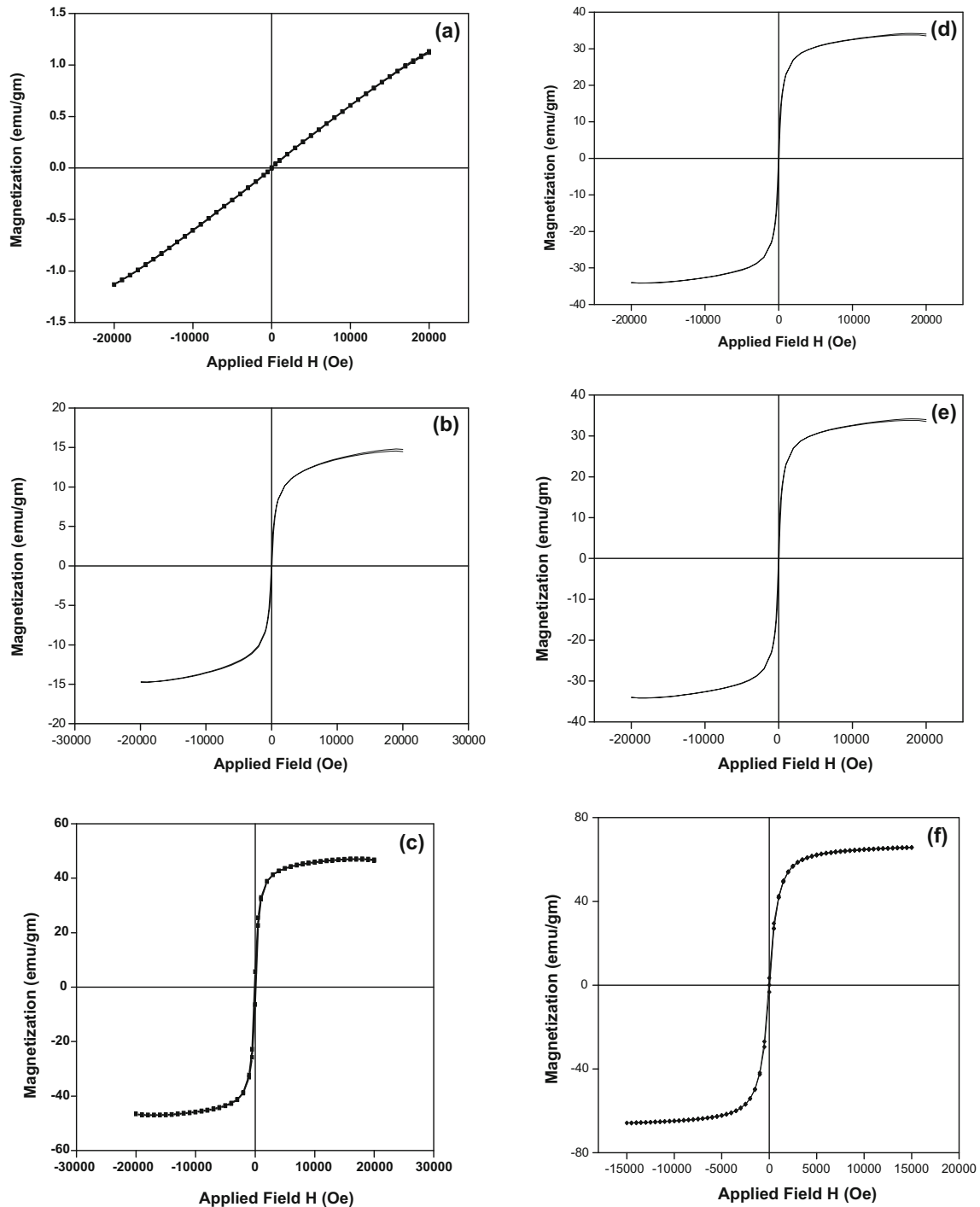


Fig. 6 Hysteresis loops of $\text{Ni}_{0.5}\text{Zn}_{0.5}\text{Fe}_2\text{O}_4$ samples as-prepared **a** coprecipitation-S1, **b** sol-gel-S2, **c** citrate gel-S3 and sintered at 1073 K **d** coprecipitation-S1 **e** sol-gel S2 **f**, and citrate gel S3 methods

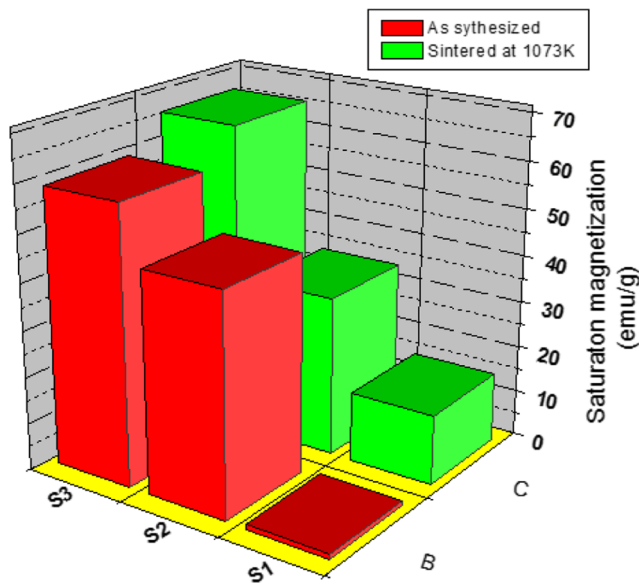


Fig. 7 Saturation magnetization of $\text{Ni}_{0.5}\text{Zn}_{0.5}\text{Fe}_2\text{O}_4$ as synthesized and sintered at 1073 K prepared via. Coprecipitation (S1), sol-gel (S2), and citrate-gel auto combustion (S3) methods

the octahedral complex other than Fe^{3+} ion. In case of as-prepared samples, it is observed that (Fig. 4) the low and high frequency absorption bands are present in S2 and S3 samples and are absent in S1 sample. Comparing Figs. 1, 2, 4, and 5 one can conclude that sintering is a prerequisite to obtain spinel phase for the samples prepared through coprecipitation route, whereas for sol-gel and citrate-gel methods do not require calcinations/sintering for the formation of spinel phase. Among the three methods, chemical coprecipitation has overriding advantages such as ease of preparation, composition flexibility, and homogeneity of the particle size, but it requires additional heat treatment to obtain the desired ferrite.

3.5 Magnetization Studies

Figure 6 depicts the room temperature hysteresis loops of as prepared (Fig. 6a–c) and sintered (Fig. 6d–f) Ni–Zn ferrite samples. It can be seen that magnetization increases with increasing applied field and reaches to a maximum

value for the samples S2 (Fig. 6c, d) and S3 (Fig. 6e, f), whereas this behavior was not observed for as-prepared S1 (Fig. 6a) sample. A decrease in magnetization (Fig. 6d) was observed for S2 sample after sintering. Figure 7 depicts the saturation magnetization of as prepared and sintered nickel-zinc ferrites prepared through coprecipitation, sol-gel, and citrate-gel methods. In general, saturation magnetization is expected to increase when the samples are sintered at higher temperatures due to the increase in grain growth and improvement in structural homogeneity. In contrary, a decrease in saturation magnetization in S2 sample is due to the redistribution of metal ions over tetrahedral (A) and octahedral (B) sites from their usual site preference. In Ni–Zn ferrite, all the Zn^{2+} ions are located at A sites only due to sp^3 hybridization and due to high crystal field stabilization Ni^{2+} ions occupy octahedral sites, while the Fe^{3+} ions are distributed among both sites [15]. Several authors reported that the deviation in the site preference of the cations at nanoscale firmly depends on the method of preparation [16–18]. The migration of Zn^{2+} from A to B sites and possible relocation of the equal number of Fe^{3+} ions from the B to A sites would generate large alteration in the exchange interaction mechanism among the cations on A and B sites. Such a possibility should increase the lattice strain compared to that as prepared sample and is apparent from the measurements from Williamson-Hall plots (Table 1). Such possibility decreases the B sublattice magnetic moment while the magnetic moment of A sublattice increases and thereby the total magnetic moment of the spinel lattice which is just the difference of the magnetic moments of the B and A sites would decrease and thus reducing the total magnetization of sample. This results in the observed decrease in magnetization. Table 3 shows the saturation magnetization, coercivity of as-prepared and sintered samples. It is clear that Ni–Zn ferrite synthesized through citrate-gel (S3) method yields highest magnetization over coprecipitation (S1) and sol-gel (S2) methods. The values of coercivity (H_c) and remanent magnetization (M_r) for all the samples obtained from the hysteresis loops and are given in Table 3. It is observed that coercivity and remanent magnetization increases with increasing sintering temperature. In addition, the coercivity of all the samples is in the range of few hundreds of Oersteds, which indicates

Table 3 Saturation magnetization (M_s), coercivity (H_c), remanent magnetization (M_r) and Resistivity of $\text{Ni}_{0.5}\text{Zn}_{0.5}\text{Fe}_2\text{O}_4$ samples (S1 coprecipitation, S2 sol-gel, S3 citrate-gel method)

Sample	M_s (emu/g)		H_c (G)		M_r (emu/g)		Grain size (μm)	Resistivity ($\Omega\text{-m}$)
	As prepared	1073 K	As prepared	1073 K	As prepared	1073 K	1073 K	313 K
S1	–	15	–	57	–	1	0.59	5.1×10^7
S2	47	34	103	47	6	3	1.02	4.4×10^7
S3	59	66	49	55	2	4	0.71	6.94×10^{10}

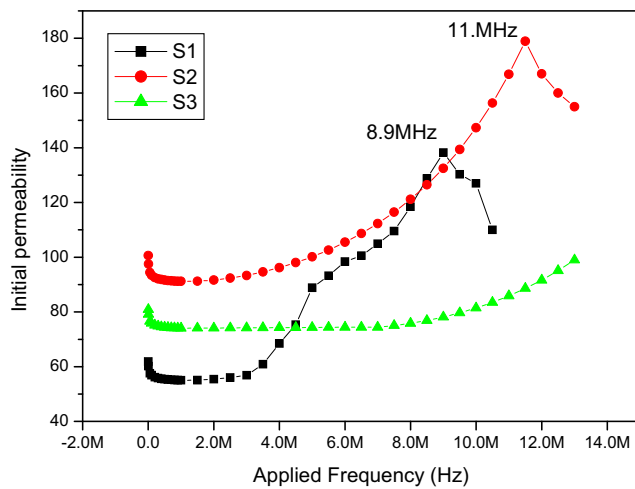
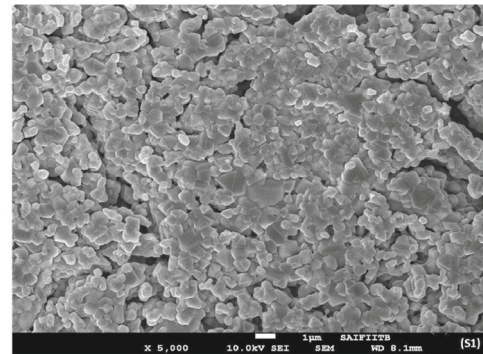


Fig. 8 Permeability as a function of frequency of $\text{Ni}_{0.5}\text{Zn}_{0.5}\text{Fe}_2\text{O}_4$ S1 coprecipitation, S2 sol-gel, and S3 citrate gel method

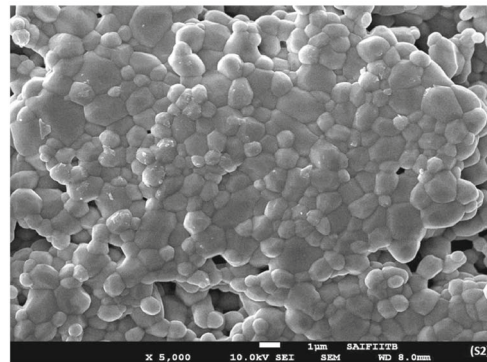
the soft character of these ferrites [19]. Globus reported that low coercive field is a necessary requirement for EM materials [20].

A stable and reasonably high value of permeability over wide operating frequency range and time is required for core applications. This is due to the fact that increasing the operating frequency of the core, the energy losses evolve as heat and increase the temperature of the core, which results in detrimental effects and thus limiting the operating range of the core. Figure 8 shows the initial permeability of Ni–Zn ferrite samples sintered at 1073 K. The initial permeability has been observed to be a nearly constant in the frequency range of 1 kHz to about 4 MHz above which a relaxation nature was noticed at 8.9 and 11 MHz for the samples S1 and S2, respectively. Usually for Ni–Zn ferrite, the initial permeability remains more or less constant with frequency until certain frequency above which the permeability decreases by a relaxation process. In case of the S3 sample, permeability was found to be stable up to 10 MHz and increases with increasing frequency. The relaxation peak was not observed in S3 sample within the experimental range. In general, permeability of ferrites depends largely on the grain size, sintered density, porosity, and magnetic anisotropy. Larger grains in the microstructure are coupled with more number of domain walls and hence, domain wall motion, which primarily contributes to initial permeability is largely enhanced. On the other hand, smaller grains are associated with more number of grain boundaries such that domain wall motion is not feasible and the presence of numerous grain boundaries acts as domain wall impediments which reduce the permeability of the sample. In addition to the above, presence of pores also restricts the domain wall motion. Since, pores will act as a source of pinning sites. The stable frequency is a desirable

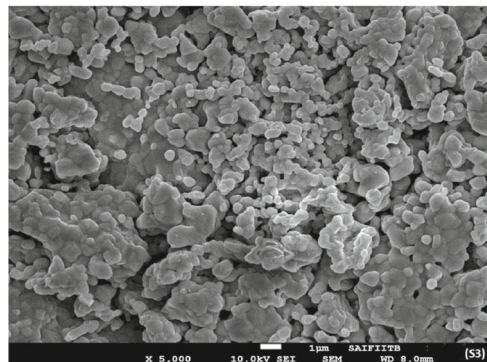
characteristic for electromagnetic applications and the flat frequency region is known as “zone of utility of ferrite” [21]. Figure 9 shows the scanning electron microscope (SEM) images of $\text{Ni}_{0.5}\text{Zn}_{0.5}\text{Fe}_2\text{O}_4$ samples synthesized through coprecipitation, sol-gel, and citrate-gel methods. It consists of large number of grains with different sizes and irregular shapes. It is observed that grains are more or less uniform in sample S2. The average grain size is estimated from the liner intercept technique. A random straight line is drawn through the micrograph. The number of grain boundaries



(a)



(b)



(c)

Fig. 9 SEM images of $\text{Ni}_{0.5}\text{Zn}_{0.5}\text{Fe}_2\text{O}_4$ samples sintered at 1073 K synthesized through **a** coprecipitation, **b** sol-gel, and **c** citrate-gel method

intersecting the line is counted. The average grain size is found by dividing the number of intersections by the actual line length. The calculated values are listed in Table 3.

3.6 DC Electrical Resistivity

The room temperature (313 K) DC electrical resistivity values of Ni–Zn ferrite sintered at 1073 K are shown in Table 3. The DC resistivity of S3 sample in the present study was noticed to be a few orders higher than the Ni–Zn ferrite prepared by the ceramic process [22]. This observation can be attributed to the presence of fine grains in the microstructure. Figure 8c shows the SEM micrograph of S3 sample. These grain boundaries are regions of mismatch between the energy states of neighboring grains and therefore act as a barrier to the flow for electrons [23]. In addition, the grain boundaries are a large source of lattice defects, inclusions, and dislocations, which perpetually reduce the grain-to-grain contact area and lessen the conductivity through the grains by increasing the scattering at grain boundaries [24]. Another advantage of fine-grained microstructure in Ni–Zn ferrite is controlling the formation of Fe^{2+} ions since the oxygen ions move faster in the smaller grains [25, 26] and thus increasing the possibility for the iron ions to remain in Fe^{3+} states.

4 Conclusions

The mixed Ni–Zn ferrite samples are prepared successfully by using three wet chemical methods. The x-ray diffraction patterns confirmed the formation of single-phase spinel structure, which indicates the presence of cations into their respective sites. Infrared spectra also confirm the formation spinel phase. It is of value to note that formation of nano-crystalline phase without subsequent thermal treatment for the samples synthesized through sol-gel (S2) and citrate-gel (S3) methods is quite appropriate and economical for large-scale industrial production. Sintering is required for the samples prepared through coprecipitation method. $\text{Ni}_{0.5}\text{Zn}_{0.5}\text{Fe}_2\text{O}_4$ sample (S3) prepared through citrate-gel autocombustion method possess highest saturation magnetization 66 emu/g (when sintered at 1073 K), electrical resistivity and with stable permeability than the other samples (S2, S3) synthesized via coprecipitation and sol-gel methods.

Compliance with Ethical Standards

Conflict of Interests The authors declare that they have no conflict of interest.

References

- Snelling, E.C.: Soft Ferrites: Properties and their application. Butterworth, London (1988)
- Verma, A., Goel, T.C., Mendiratta, R.G., Gupta, R.G.: J. Magn. Magn. Mater. **192**, 271 (1999)
- Wang, C., Liu, S., Liu, L., Bai, X.: Mater. Chem. Phys. **96**, 361 (2006)
- Raul, V.: Phys. Res. Inter. **ID 591839**, 9 (2012)
- Yue, Z., Zhou, J., Li, L., Gui, Z.: J. Magn. Magn. Mater. **233**, 224 (2001)
- Chen, D.G., Tang, X.G., Wu, J.B., Zhang, W., Liu, Q.X., Jiang, Y.P.: J. Magn. Magn. Mater. **323**, 1717 (2011)
- Zahi, S., Hashim, M., Daud, A.R.: J. Magn. Magn. Mater. **308**, 177 (2007)
- Bhaskar, A., Kanth, B.R., Murthy, S.R.: J. Magn. Magn. Mater. **283**, 109 (2004)
- Li, X., Wang, G.: J. Magn. Magn. Mater. **32**, 12761 (2009)
- Nelson, J.B., Riley D.P.: Proc. Phys. Soc. **57**, 160 (1945)
- Cullity, B.D., Stock, S.R.: Principles of x-ray diffraction. Prentice Hall Inc. (2001)
- Neena Sugathan, B., Vrinda, V., Salini, S.L.: J. Mater. Sci. **43**, 1175 (2008)
- Weil, L., F., Bertaut Bochirol, L.: J. Phys. Radium. **11**, 208 (1950)
- Waldron, R.D.: Phys. Rev. **99**, 1727 (1955)
- Siva Ram Prasad, M., Prasad, B.B.V.S.V., Rajesh, B., Rao, K.H., Ramesh, K.V.: J. Magn. Magn. Mater. **323**, 2115 (2011)
- Beji, Z., Smiri, L.S., Yaacoub, N., Grenèche, J.-M., Menguy, N., Ammar, S., Fiévet, F.: Chem. Mater. **22**, 1350 (2010)
- Gubbala, S., Nathani, H., Koizol, K., Misra, R.D.K.: Phys. B. **348**, 317 (2004)
- Thakur, S., Katyal, S.C., Gupta, A., Reddy, V.R., Sharma, S.K., Knobel, M., Singh, M.: J. Phys. Chem. C **113**, 20785 (2009)
- Ahmad, M., Grossinger, R., Ali, I., Ahmad, I., Rana, M.U.: J. Alloys Comp. **577**, 382 (2013)
- Globus, A., Pascard, H., Cagan, V.: J. Phys. Symp. **38**, C1–163 (1977)
- Verma, A., Goel, T.C., Mendiratta, R.G., Gupta, R.G.: J. Magn. Magn. Mater. **192**, 271 (1999)
- Rezlescu, E., Sachelarie, L., Popa, P.D., Rezlescu, N.: IEEE Trans. Magn. **36**, 3962 (2000)
- Shinde, T.J., Gagkari, A.B., Vasambekar, P.N.: Mater. Chem. Phys. **111**, 87 (2008)
- Nikumbh, A.K., Nagawade, A.V., Gugale, G.S., Chaskar, M.G., Bakare, P.P.: J. Mater. Sci. **37**, 637 (2002)
- Batoo, K.M., Kumar, S., Lee, C.G., Alimuddin: Current Appl. Phys. **9**, 1072 (2009)
- Thakur, A., Mathur, P., Singh, M.: J. Phys. Chem. Sol., 68 (2007)